Dual-Responsive Nanoreactor Initiates In Situ Generation of Copper Complex for Paraptosis-Mediated Tumor Chemo-Immunotherapy

Mei-Ting Niu, Qian-Ru Li, Qian-Xiao Huang, Lin-Meng Liu, You-Teng Qin, Chao-Yan Wu, Si-Xue Cheng, and Xian-Zheng Zhang*

Paraptosis is a non-apoptotic and caspase-independent programmed cell death that can trigger immunogenic cell death (ICD) in tumor cells, representing a potent tactic to overcome immune tolerance to apoptosis. Here, this study demonstrates the construction of a dual-responsive nanoreactor (MCGDH) to achieve paraptosis-mediated ICD for chemo-immunotherapy. Specifically, by doping Cu^{2+} into glutathione (GSH)-responsive dendritic mesoporous silica nanoparticles, the platform (CGDMSN) is endowed with partial acid-sensitivity. After loaded with 8-hydroxyquinoline (8-HQ), cell membrane fragments are coated onto the ammoniated CGDMSN surface to construct MCGDH. Upon internalization by tumor cells, the release of Cu^{2+} and 8-HQ from MCGDH in response to the acidic pH and high concentration of GSH in the tumor microenvironment stimulates in situ generation of $Cu(8-HQ)_2$, inducing tumor cells paraptosis at a low copper dose. Moreover, MCGDH-mediated paraptosis amplifies the immunogenicity of tumor cells, facilitating antigen presentation to dendritic cells and activating $CD8^+/CD4^+$ T cells immune responses. Furthermore, the combination of MCGDH and anti-PD-1 antibodies (αPD-1) promotes the systemic anti-tumor immune responses and long-term immunological effect to vastly inhibit the primary/distant tumor growth and prevent tumor metastasis. This GSH/pH dual-responsive nanoreactor serves as a selective platform for accelerating the development of chemo-immunotherapy.

1. Introduction

Immunotherapy offers promising alternatives or complementary options to traditional chemotherapy. However, chemotherapy continues to be the first-line treatment for the most malignant tumors in clinical practice.[1] Unfortunately, the mechanism of routine chemotherapeutics often involves apoptotic pathway, which commonly leads to immune tolerance in tumor cells,[2] thus limiting the further development of anti-tumor chemo-immunotherapy. In recent years, researchers have increasingly focused on non-apoptotic regulated cell deaths, which may be a key manager to improve the immunogenicity of tumor cells for amplified immune responses.[2b,3] Paraptosis is a type of non-apoptotic and caspase-independent programmed cell death, whose morphological features are extensive cytoplasmic vacuolation and mitochondrial/endoplasmic reticulum (ER) swelling.[4] It relies on de novo protein synthesis and is characterized by ER stress and reactive oxygen species (ROS) production,[5] which are the crucial approaches for the induction of immunogenic cell death (ICD),[6] reasoning that paraptosis-triggered ICD could serve as an effective anti-tumor immunotherapy booster.[5a,7] More importantly, the immune responsiveness of T cells mediated by ICD enhances the clinical response rate effectiveness of immune checkpoint blockade (ICB) therapy.[8] Recently, some metal-based complexes, such as iridium (Ir)-/ruthenium (Ru)-/copper (Cu)-based complexes have been reported to eliminate tumor cells through the paraptosis pathway.[9]
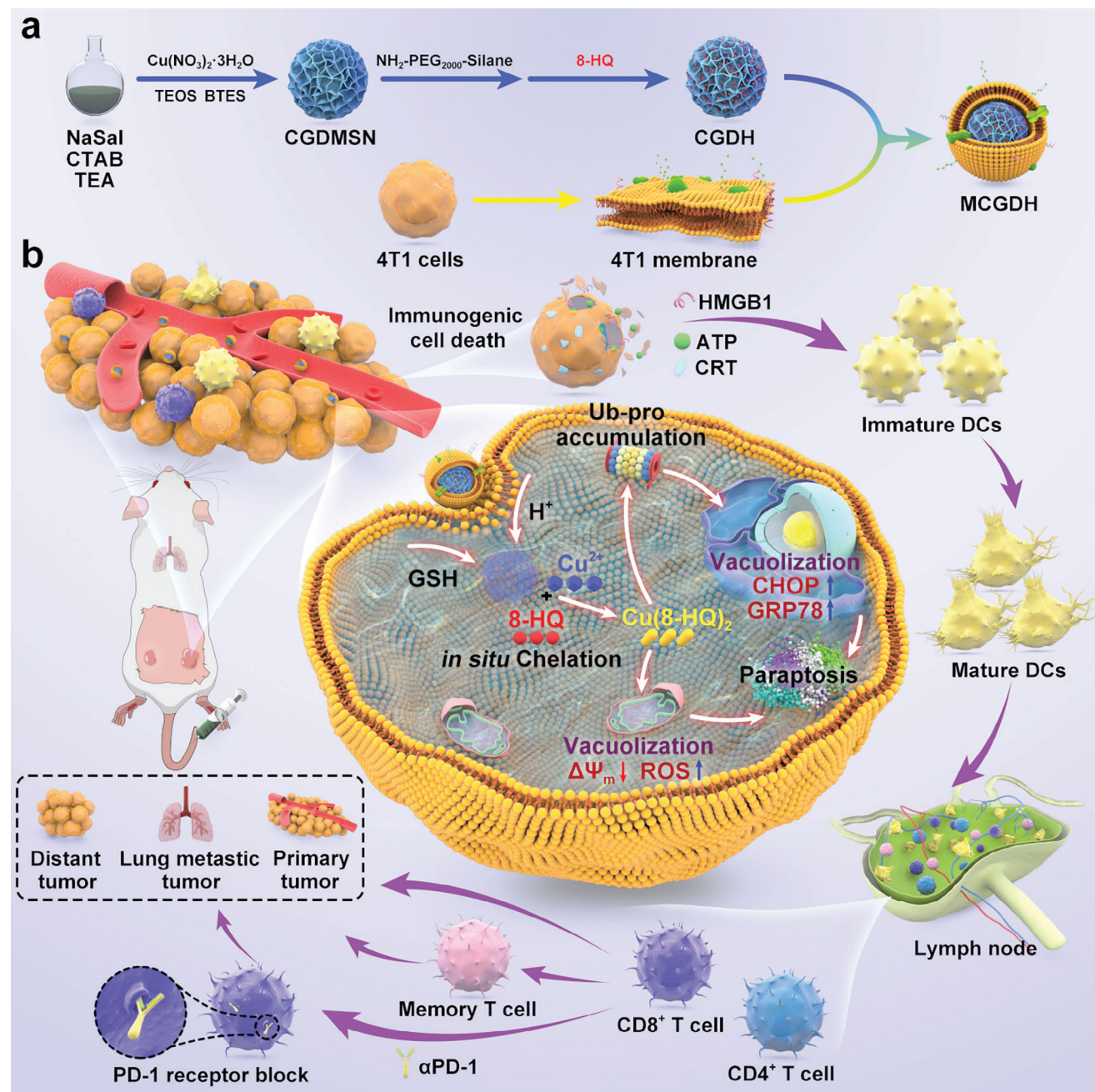
Cu is a vital trace element for all living organisms, and participates in various biological pathways.[10] It has been utilized to inhibit tumor growth via cell apoptosis, cuproptosis or paraptosis by disrupting Cu homeostasis in tumor cells.[9c,11] However, the development of Cu-based metallodrugs is significantly hindered by the systemic toxicity caused by excessive exogenous copper.[12] Therefore, it is imperative to investigate the utilization of low-dose copper for achieving potent eradication of tumor cells. As a promising novel drug candidate for anti-tumor therapy,

M.-T. Niu, Q.-R. Li, Q.-X. Huang, L.-M. Liu, Y.-T. Qin, S.-X. Cheng,
X.-Z. Zhang
Key Laboratory of Biomedical Polymers of Ministry of Education &
Department of Chemistry
Wuhan University
Wuhan 430072, P. R. China
E-mail: xz-zhang@whu.edu.cn
C.-Y. Wu, X.-Z. Zhang
Department of Traditional Chinese Medicine
Zhongnan Hospital
Wuhan University
Wuhan 430071, P. R. China

**ADVANCED
SCIENCE NEWS**

www.advancedsciencenews.com

**ADVANCED
FUNCTIONAL
MATERIALS**

www.afm-journal.de

Scheme 1. Schematic illustration of MCGDH-mediated paraptosis for chemo-immunotherapy. a) Preparation process of MCGDH. b) Mechanism of immunogenic cells death via paraptosis pathway caused by MCGDH and subsequent series of active immune responses.

8-Hydroxyquinoline (8-HQ) exhibits a strong affinity for Cu^{2+}, and can form the complex $Cu(8-HQ)_2$, which has been shown to induce tumor cell death through the paraptosis pathway.[13] Besides, $Cu(8-HQ)_2$ exhibits a superior cytotoxic effect against various tumor cells (Figure S1, Supporting Information), indicating the remarkable efficacy of lower-dose copper in eradicating tumor cells. However, the further application of $Cu(8-HQ)_2$ has been restricted due to its low target selectivity to tumor cells during administration. Fortunately, the employment of nanomedicine for in situ synthesis of $Cu(8-HQ)_2$ in the tumor

microenvironment (TME) holds great promise for precise anti-tumor therapy.[14]

Here, a Cu-based nanoreactor has been developed to induce tumor cell paraptosis, which is promising to trigger superior immunogenic cell death (ICD) and anti-tumor immune response (**Scheme 1**). Cu^{2+} is doped into dendritic glutathione (GSH)-responsive dendritic mesoporous silica nanoparticles (designated as CGDMSN) via Cu—O bond, preventing Cu^{2+} leakage during delivery and endowing the nanoparticle with partial acid-sensitivity to expedite the biodegradation of the -Si-O-Si-

**ADVANCED
SCIENCE NEWS**

www.advancedsciencenews.com

**ADVANCED
FUNCTIONAL
MATERIALS**

www.afm-journal.de

framework under acidic condition.[15] Besides, the disintegration process consumes antioxidative GSH to some extent, which has been reported to contribute to improve anti-tumor effect.[16] After loaded with 8-HQ, the nanoplatform is coated with 4T1 tumor cell membrane fragments (CMs) to obtain the dual-responsive Cu-based nanoreactor (designated as MCGDH) for fantastic tumor homologous targeting ability and biocompatibility.[17] When internalized by 4T1 tumor cells, Cu^{2+} and 8-HQ will be released with MCGDH decomposition, and then a preferential coordination reaction of them is performed for in situ production of paraptosis inducer $Cu(8-HQ)_2$.[18] Subsequently, paraptosis-mediated ICD releases abundant molecular patterns (DAMPs) and tumor associated antigens (TAAs) to promote the maturation of dendritic cells (DCs) and the activation of the $CD8^+/CD4^+$ T cells.[19] Furthermore, the in vivo studies validated that the combination of MCGDH and immune checkpoint inhibitor anti-PD-1 antibodies (αPD-1) encouraged the systemic anti-tumor immune responses and long-term immunological effects to inhibit the primary/distant tumors and avoid tumor metastasis. In summary, this dual-responsive nanoreactor provides a promising strategy for accelerating the development of chemo-immunotherapy through paraptosis pathways.

2. Results and Discussion

2.1. Synthesis and Characterization of Nanoparticles

The synthesis process of MCGDH is presented in **Scheme 1a**. CGDMSN was prepared by a modified hydrothermal synthesis approach.[20] The nitrogen adsorption/desorption isotherm and corresponding pore size distribution verified the large specific surface area and mesoporous size (477.6 $m^2 g^{-1}$, 6.6 nm) of CGDMSN (Figure S2, Supporting Information), validating its potential as an excellent drug carrier. Then the amino groups on the surface of CGDMSN were modified through NH_2-PEG_{2000}-Silane (designated as CGDMSN-NH_2) to facilitate the camouflage of CMs. After surface amination, 8-HQ was loaded into CGDMSN-NH_2 to obtain CGDH-NH_2. And MCGDH was synthesized by coating CMs onto CGDMSN-NH_2 through electrostatic interactions and physical extrusion. The loading of 8-HQ into CGDMSN was denoted as CGDH, with the 8-HQ loading amounts in CGDH and MCGDH being $\approx$12.81 $\pm$ 1.06% and 9.98 $\pm$ 1.32%, respectively (Figure S3, Supporting Information). Transmission electron microscopy (TEM) images depicted the dendritic and spherical morphology of CGDH, with a diameter of $\approx$105 nm. Upon assembly into MCGDH, the size kept almost the same, but the dendritic morphology became obscured due to the coating of CMs on the surface (**Figure 1a,b**). The hydrodynamic diameters of CGDMSN, CGDH-NH_2 and MCGDH were found to be roughly 234.7, 292.2, 293.6 nm with the polydispersity index (PDI) of 0.115, 0.144, 0.139, respectively, based on the dynamic light scattering (DLS) data. This was caused by the extended PEG chains on the surface of CGDH-NH_2 and the presence of CMs coating on MCGDH (Figure 1c). The zeta potential changed from −36.5 to + 9.7 to −22.7 mV, indicating the successful modification of amino groups on CGDMSN and the coating of CMs (Figure 1d). Data of hydrodynamic diameter, PDI and zeta potential were monitored within 7 days, which verified the stability of MCGDH (Figure 1i; Figure S4, Supporting Information).

The energy dispersive X-ray (EDX) spectra exhibited the presence of Si, O, S, Cu in CGDH and Si, O, S, Cu, P in MCGDH (Figure 1e,f). Sodium dodecyl sulfate polyacrylamide gel electrophoresis (SDS-PAGE) demonstrated that the CMs proteins were intactly remained in MCGDH (Figure 1g). Confocal laser scanning microscopy (CLSM) images demonstrated a complete overlap of the green fluorescence labeled on CMs (designated as CMs-FITC) and the red fluorescence linked to CGDMSN-NH_2 (designated as CGD-Cy5.5) outside the cell nuclei, revealing MCGDH could maintain integrated structure after being internalized by 4T1 cells (Figure 1h). Subsequently, the biodegradation of MCGDH by GSH and acid in vitro was studied. As shown in Figure 1j, after 72 h, the morphology of MCGDH was essentially intact at pH 7.4 without GSH but was partially damaged in the presence of 10 mM GSH or under acidic environment (pH 5.5). While the morphology of MCGDH was nearly completely disintegrated in the imitative intracellular microenvironment (GSH 10 mM, pH 5.5). In addition, the released behavior of Cu^{2+} (Figure S5, Supporting Information) and 8-HQ (Figure 1k) from MCGDH were consistent with the degradation behavior of MCGDH.

Then, CMs-coated dendritic mesoporous silica loaded with 8-HQ (abbreviated as MDH) and CMs-coated and glutathione-depleted dendritic mesoporous silica loaded with 8-HQ (abbreviated as MGDH) were synthesized as control groups for subsequent studies. In contrast with the dark green color of CGDMSN, dendritic mesoporous silica (abbreviated as DMSN) nanoparticles and glutathione-depleted dendritic mesoporous silica (abbreviated as GDMSN) nanoparticles appeared as milk-white when dispersed in water (Figure S6, Supporting Information). TEM images showed both DMSN and GDMSN exhibited a dendritic and spherical morphology, with diameters of $\approx$200 and 115 nm, respectively (Figure S7a,b, Supporting Information). The Si, O elements of DMSN and Si, O and S of GDMSN were verified by EDX spectrum (Figure S7c,d, Supporting Information). Notably, the dendritic morphology of CGDMSN was somewhat deficient as compared with DMSN or GDMSNN as shown in TEM images (Figure 1a; Figure S7a,b, Supporting Information). Compared with CGDMSN (477.6 $m^2 g^{-1}$, 6.6 nm), the nitrogen adsorption/desorption isotherm and corresponding pore size distribution of DMSN (436.6 $m^2 g^{-1}$, 15.0 nm) and GDMSN (428.8 $m^2 g^{-1}$, 15.3 nm) exhibited smaller specific surface areas and larger pore sizes (Figure S2, Supporting Information). X-ray powder diffraction (XRD) patterns exhibited that the amorphous structure of DMSN and GDMSN was the same as that of CGDMSN (Figure S8, Supporting Information). The hydrodynamic diameters of DMSN, ammoniated dendritic mesoporous silica (DMSN-NH_2), MDH were measured to be $\approx$281.0, 331.8, 336.6 nm, with PDI of 0.080, 0.173, 0.102, respectively (Figure S9a, Supporting Information). For GDMSN, ammoniated and glutathione-depleted dendritic mesoporous silica GDMSN-NH_2, MGDH, the hydrodynamic diameters were $\approx$225.4, 297.0, 300.7 nm, with PDIs of 0.081, 0.117, 0.167, respectively (Figure S9c, Supporting Information). The zeta potentials of DMSN, DMSN-NH_2, MDH were −24.2, + 7.45 and −13.2 mV, respectively (Figure S9b, Supporting Information), and the zeta potentials of GDMSN, GDMSN-NH_2, MGDH were −30.4, + 14.0, −17.6 mV, respectively (Figure S9d, Supporting Information), indicating the successful preparation of MDH and MGDH. The 8-HQ loading

ADVANCED
SCIENCE NEWS
www.advancedsciencenews.com

ADVANCED
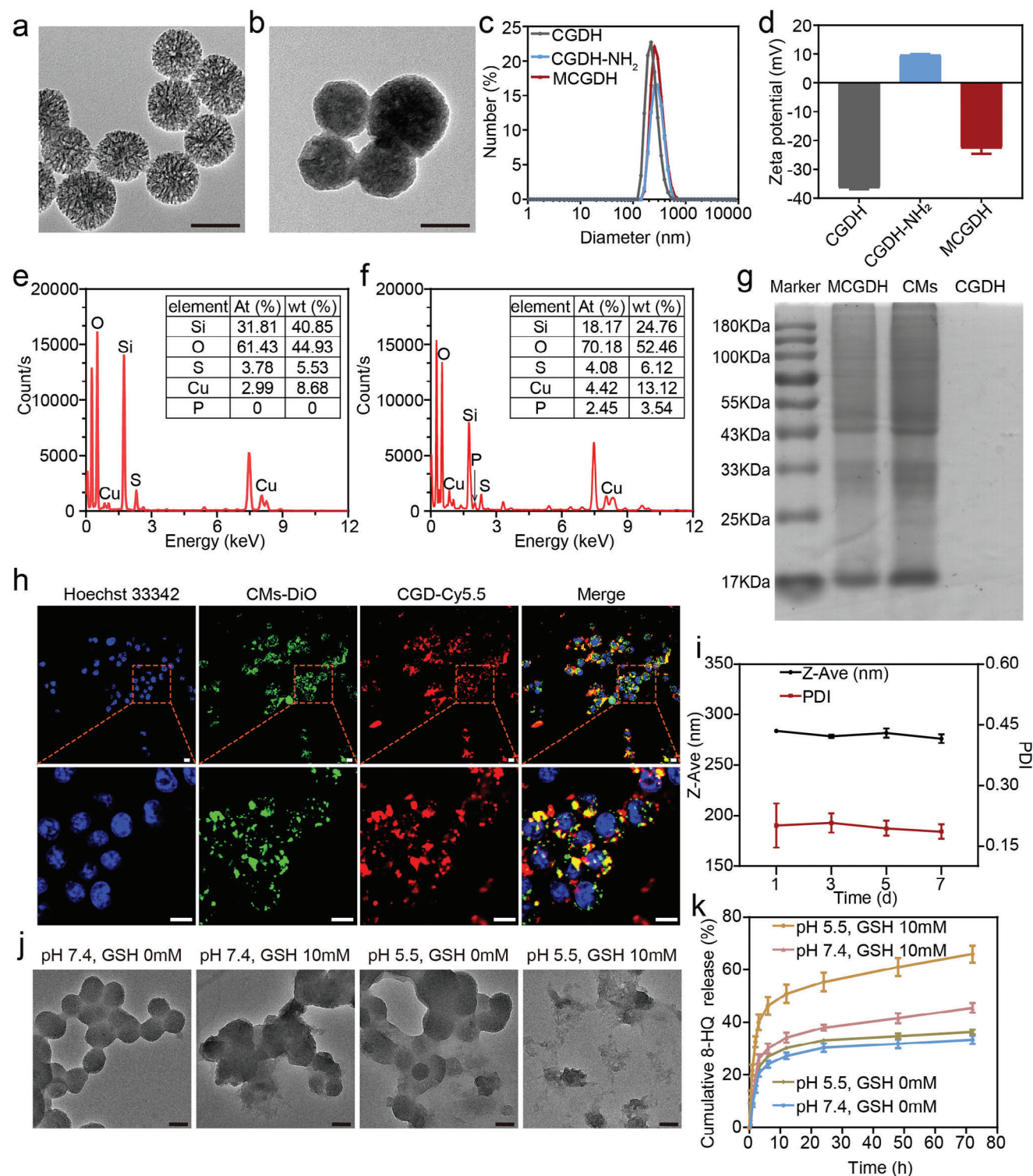FUNCTIONAL
MATERIALS
www.afm-journal.de

Figure 1. Characterization of CGDH and MCGDH. The TEM images of a) CGDH and b) MCGDH. Scale bar: 100 nm. c) The hydrodynamic diameters and d) the zeta potentials of CGDH, CGDH-NH$_2$, and MCGDH (n = 3). The EDX spectra of e) CGDH and f) MCGDH. g) SDS-PAGE protein assay of MCGDH, CMs and CGDH. h) CLSM images of colocalization of MCGDH in 4T1 cells. Cell nucleus, CMs and CGDMSN-NH$_2$ were labeled with Hoechst33342 (blue), DiO (green), and Cy5.5 (red), respectively. Scale bar 10 μm. i) Evaluation of stability regarding hydrodynamic diameters and PDI. j) The representative TEM images of MCGDH in different conditions. Scale bar: 100 nm. k) Cumulative release of 8-HQ from MCGDH incubated under different conditions (n = 3). Data are represented as mean values ± SD.

**ADVANCED
SCIENCE NEWS**

www.advancedsciencenews.com

**ADVANCED
FUNCTIONAL
MATERIALS**

www.afm-journal.de

amounts of MDH and MGDH were $\approx 8.58 \pm 1.39\%$ and $7.49 \pm 1.73\%$, respectively (Figure S3, Supporting Information).

2.2. In Vitro Validation of the Mechanism of MCGDH-Mediated 4T1 Tumor Cells Paraptosis

The uptake of MCGGH by 4T1 tumor cell were evaluated by CLSM and flow cytometry (FCM) analysis. The green fluorescence intensity of fluoresceinisothiocyanate (FITC)-labeled MCGDH was observably stronger than that of FITC-labeled CGDH (**Figure 2**a–c), displaying the enhanced endocytosis efficiency due to the homologous targeting abilities of CMs. Since the cleavage of S—S bond involves complex reactions associated with GSH, the content of intracellular GSH was evaluated.[21] Compared with 4T1 cells that treated with PBS or DMSN, the GSH level in 4T1 cells decreased in a time-dependent manner after treatment with GDMSN or CGDMSN (Figure 2d). Afterwards, the cytotoxicity of different nanoparticles in 4T1 tumor cells was determined by MTT assay. DMSN showed negligible cytotoxicity, while GDMSN and CGDMSN exhibited only 90% and 80% cytotoxicity even at a concentration of 108 µg mL^{-1}, respectively (Figure 2e), suggesting that the sole depletion of intracellular GSH by the oxidation of tetrasulfide bond and the incorporation of Cu^{2+} (16.0 µM) in CGDMSN (108 µg mL^{-1}) were insufficient to induce obvious tumor cell death. By the way, the content of Cu^{2+} in CGDMSN was determined based on the results obtained from ICP-MS analysis (Table S1, Supporting Information). After loaded with 8-HQ, the cytotoxicity of CGDH and MCGDH to 4T1 cells increased significantly with the increase of concentration, but MDH and MGDH did not demonstrate the same cytotoxic effect (Figure 2f), suggesting that the sole release of 8-HQ was insufficient to induce effective cytotoxicity, while the simultaneous release of Cu^{2+} and 8-HQ could trigger rapid cell death. To verify whether the cytotoxicity of MCGDH to 4T1 cells was indeed attributed to the in situ formation of Cu(8-HQ)$_2$, the cytotoxicity of free Cu^{2+} (equal to the copper content in MCGDH), MDH + Cu^{2+}, MGDH, CGDH and MCGDH was evaluated. As depicted in Figure 2g, free Cu^{2+} and MGDH did not demonstrate remarkable cytotoxic effect, while the cytotoxicity of MDH + Cu^{2+} to 4T1 cells increased significantly, though not as that pronounced as CGDH and MCGDH, confirming that MCGDH, acting as a dual-responsive nanoreactor, exerted a substantial cytotoxic effect on 4T1 cells at the low-dose of copper and 8-HQ through chelation reactions. All these results collectively indicated that MCGDH served as an effective platform for the eradication of tumor cells.

Afterwards, to confirm whether MCGDH induced 4T1 tumor cells death through paraptosis, the morphological characteristics of 4T1 cells after different treatments were observed through Bio-TEM images. As depict in Figure 2h, the cytoplasm, ER and mitochondria of 4T1 cells showed more obviously typical vacuolization in the MDH + Cu^{2+}, CGDH and MCGDH groups than the other three groups. CLSM images of Mito-Tracker Green and ER-Tracker Red further verified the certain vacuolization of mitochondria and ER (Figure 2i,j). These results supported that the biodegradation-mediated in situ intracellular generation of Cu(8-HQ)$_2$ induced a paraptosis-like cell death. Then, the intracellular ROS level in 4T1 cells was assessed by DCFH-DA. The fluorescence signal of ROS was quite weak in control, Cu^{2+} and MCGH groups. While the increasing trend in fluorescence signal of ROS in MDH + Cu^{2+}, CGDH and MCGDH groups was attributed to the higher endocytosis efficiency and in situ generation of cytotoxic Cu(8-HQ)$_2$ (**Figure 3**a). The CLSM images and FCM analysis revealed a substantial increase in JC-1 monomers and decrease in JC-1 aggregates of the MDH + Cu^{2+}, CGDH and MCGDH groups (Figure 3b–f), indicating that Cu(8-HQ)$_2$-mediated paraptosis induced a decline in mitochondrial membrane potential. Previous research has reported that paraptosis is associated with ER stress caused by ubiquitin–proteasome pathway inhibition.[4b,22] The expression of the ER stress markers, CHOP and GRP78, was evidently elevated in the groups forming Cu(8-HQ)$_2$ (Figure 3g). Besides, a significant accumulation of ubiquitinated (Ub) proteins occurred in MDH + Cu^{2+}, CGDH and MCGDH groups (Figure 3h). Furthermore, the pretreatment with the de novo translation inhibitor cycloheximide (CHX) attenuated the cytotoxicity of MCGDH to 4T1 cells. While apoptosis inhibitors (Z-VAD-FMK) and necroptosis inhibitors (necrostatin-1) could not weaken MCGDH-induced cell death (Figure S10, Supporting Information). Western blot (WB) analysis displayed that there was no obvious cleavage of apoptosis-related caspased-3 and poly ADP-ribose polymerase (PARP1), nor increase in necroptosis-related kinases receptor-interacting protein 1 (RIP1) and RIP3 in the MDH + Cu^{2+}, CGDH and MCGDH groups in comparison with the control group (Figure S11, Supporting Information), implying that MCGDH-induced cell death was independent of apoptosis or necroptosis. Based on the above, it could be confirmed that MCGDH induces paraptosis in cells through in situ intracellular complexation of Cu(8-HQ)$_2$, which mediated a grievous oxidative stress and an extensive unfolded protein response, ultimately resulting in extensive vacuolation.

2.3. In Vitro Evaluation of MCGDH-Mediated ICD and DCs Maturation

To explored paraptosis-triggered ICD, the characteristic DAMPs, including adenosine triphosphate (ATP) release, extracellular migration of high-mobility group box 1 protein (HMGB1) and surface exposure of calreticulin (CRT), were detected. In detail, in the MDH + Cu^{2+}, CGDH, and MCGDH groups, the intracellular ATP levels of 4T1 cells were decreased and the HMGB1 contents in the culture supernatant were increased significantly (**Figure 4**a,b). FCM analysis and immunofluorescence staining images demonstrated that exposure of CRT on cell membrane surface was significantly higher in the MDH + Cu^{2+}, CGDH, and MCGDH groups compared to the other three groups, and the CRT positive cells of the MCGDH group were 1.3-fold of that of the MDH + Cu^{2+} group (Figure 4c–e). These results consistently suggested that MCGDH-mediated in situ intracellular generation of Cu(8-HQ)$_2$ effectively induced the ICD in 4T1 cells. Subsequently, to mimic the in vivo effect of MCGDH on DC maturation, bone-marrow-derived DCs (BMDCs) were co-incubated with the treated 4T1 cells (Figure S12, Supporting Information). The BMDCs without any treatment were used as the blank group. The mature DCs (mDCs) in the control group was 1.66-fold higher than the blank group. The percentages of mDCs were 37.3%, 44.9%, 52.3%, 51.4%, and 57.3% in the Cu^{2+}, MGDH, MDH + Cu^{2+}, CGDH and MCGDH groups, respectively

ADVANCED
SCIENCE NEWS

www.advancedsciencenews.com

ADVANCED
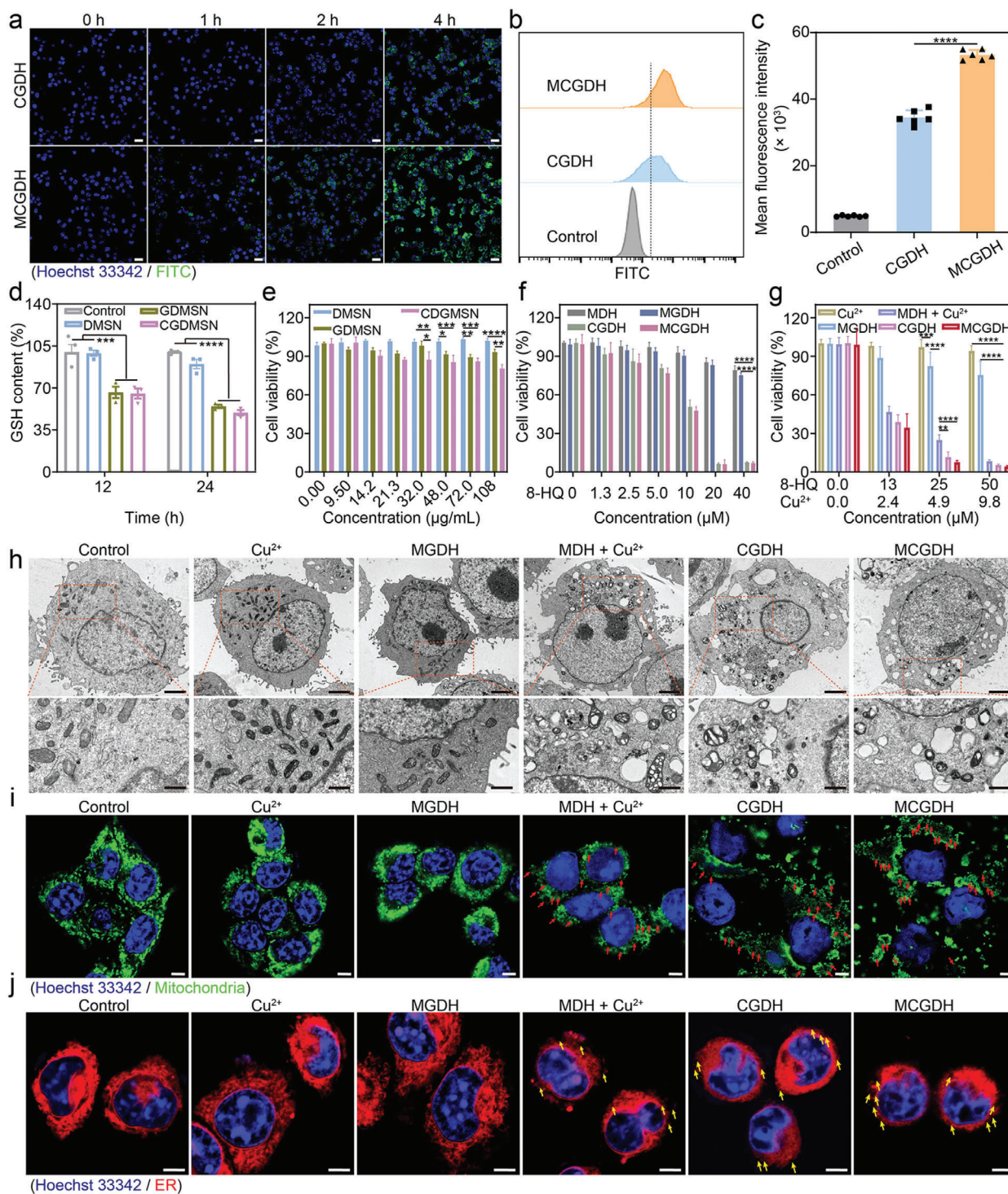**FUNCTIONAL**
MATERIALS

www.afm-journal.de

Figure 2. In vitro evaluation of MCGDH-mediated anti-tumor therapeutic effects and the morphological characteristics related to paraptosis. a) CLSM images of 4T1 tumor cells treated with FITC labeled-CGDH and FITC labeled-MCGDH for different times. Scale bar: 20 µm. b) Flow cytometry (FCM) analysis of 4T1 tumor cells treated with FITC labeled-CGDH and FITC labeled-MCGDH for 4 h (n = 6) and c) the corresponding mean fluorescence intensity (n = 6). d) GSH content of 4T1 cells after incubation with DMSN, GDMSN and CGDMSN for 12 or 24 h (n = 3). e) Cell viability of 4T1 cells after treatment with different concentrations of DMSN, GDMSN and CGDMSN for 24 h (n = 6). f) Cell viability of 4T1 cells after treatment with MDH, MGDH, CGDH and MCGDH for 24 h (n = 6). g) Cell viability of 4T1 cells after treatment with Cu^{2+}, MDH + Cu^{2+}, MGDH, CGDH, and MCGDH for 24 h (n = 6). The content of Cu^{2+} in MDH + Cu^{2+} group was equivalent to that in MCGDH, detected by ICP-MS. h) Bio-TEM images of the cross-section of 4T1 tumor cells after different treatments. Scale bar: 2 µm (up), 0.8 µm (down). CLSM images of 4T1 cells treated with virous treatments and subsequently stained by i) Mito-Tracker Green and j) ER-Tracker Red. Scale bar: 5 µm. Data are represented as mean values ± SD. Significant difference was assessed by one-way ANOVA. $^{*}p < 0.05$, $^{**}p < 0.01$, $^{***}p < 0.001$, $^{****}p < 0.0001$, n.s. no significance.

**ADVANCED
SCIENCE NEWS**

www.advancedsciencenews.com

**ADVANCED
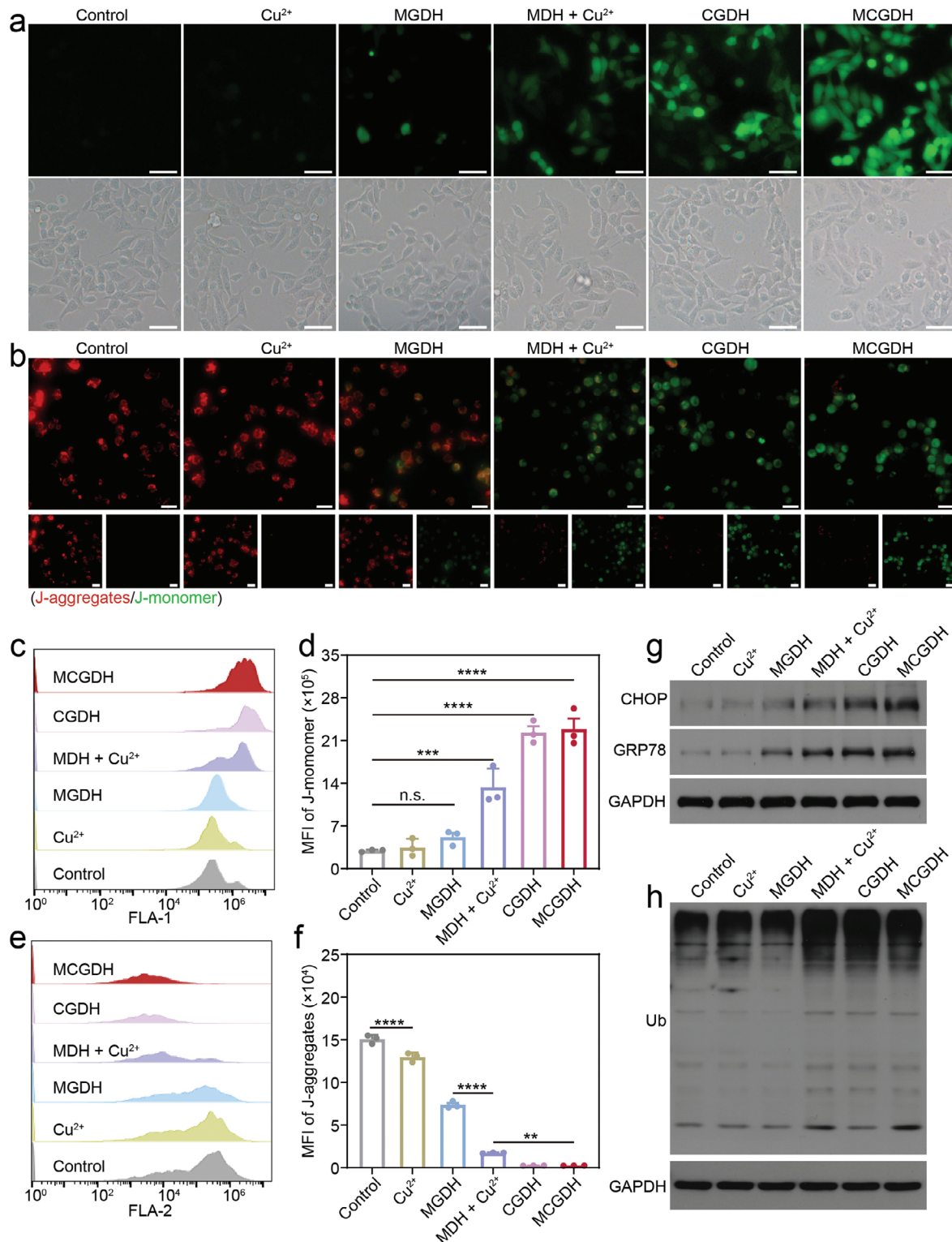FUNCTIONAL
MATERIALS**

www.afm-journal.de

Figure 3. Study on MCGDH-mediated 4T1 tumor cells paraptosis. a) CLSM images of intracellular ROS levels after different treatments. Scale bar: 50 μm b) Mitochondria membrane potential of 4T1 cells after different treatments, stained with JC-1. Scale bar: 50 μm. c) Representative histograms of J-monomer in 4T1 cells subjected to different treatments and d) corresponding quantitative fluorescence intensity analysis by FCM analysis (n = 3). e) Representative histograms of J-aggregates in 4T1 cells subjected to different treatments and f) corresponding quantitative fluorescence intensity analysis by FCM analysis (n = 3). g) Western blotting analysis of the expression of CHOP, GRP78 and h) Ub proteins in 4T1 tumor cells following different treatments. Data are represented as mean values ± SD. Significant difference was assessed by one-way ANOVA. $^*p < 0.05$, $^{**}p < 0.01$, $^{***}p < 0.001$, $^{****}p < 0.0001$, n.s. no significance.

**ADVANCED
SCIENCE NEWS**

www.advancedsciencenews.com

**ADVANCED
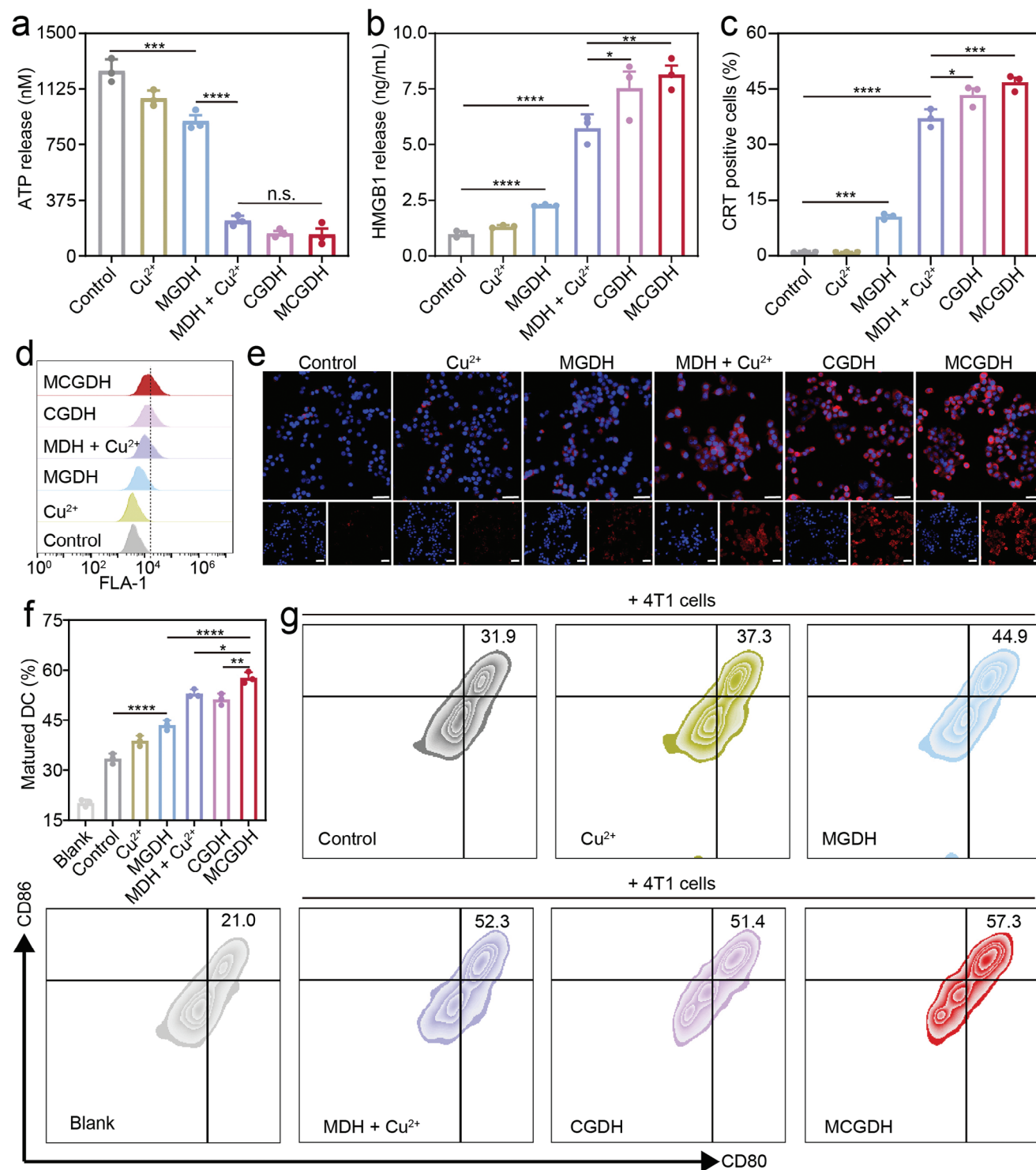FUNCTIONAL
MATERIALS**

www.afm-journal.de

Figure 4. Evaluation of paraptosis-evoked ICD and DCs maturation in vitro. a) Intracellular secretion of ATP and b) the release of HMGB1 from 4T1 cells after different treatments (n = 3). c) Quantitative analysis (n = 3) and d) corresponding representative flow cytometry plots of exposed CRT in 4T1 tumor cells. e) Immunofluorescence staining of CRT in 4T1 tumor cells subjected to various treatments. Scale bar: 200 μm. f) Quantification of mature DCs after various treatments (n = 3) and g) corresponding representative flow cytometry plots. Data are represented as mean values ± SD. Significant difference was assessed by one-way ANOVA. *$p < 0.05$, **$p < 0.01$, ***$p < 0.001$, ****$p < 0.0001$, n.s. no significance.

ADVANCED
SCIENCE NEWS
www.advancedsciencenews.com

ADVANCED
FUNCTIONAL
MATERIALS
www.afm-journal.de

(Figure 4f,g), indicating that MCGDH effectively triggered ICD and then enhanced the engulfment of TAAs by immature DCs (imDCs). The function of mDCs was further evaluated via the detection of cytokines in the supernatant of BMDCs after different treatments. The level of interleukin 6 (IL-6), tumor necrosis factor α (TNF-α) and interferon-β (INF-β) in the MCGDH-treated group increased significantly (Figure S13, Supporting Information), indicating that MCGDH-mediated ICD effectively facilitated the maturation of DCs, which thereby became a hopeful candidate to provoke anti-tumor immune responses.

2.4. In Vivo Evaluation of MCGDH-Mediated Anti-Tumor Effects and Immune Responses Mechanisms

To validate the potential of the dual-responsive nanoreactor in vivo, the biocompatibility and biosafety of MCGDH were assessed first. The hemolysis ratio of the MCGDH group was lower than that of the CGDH group at the equivalent concentration (Figure S14, Supporting Information), indicating that coating CMs endowed these nanoreactors with enhanced blood compatibility. Additionally, the blood biochemical and blood routine experiments have verified that the peripheral blood cell indexes, liver function-involved enzymes and kidney function-associated biomarkers in each group were maintained in a stable range (Figure S15, Supporting Information), proclaiming the therapeutic formulations had negligible acute systemic toxicity and would not cause liver or renal function injury. Besides, H&E staining assays revealed no significant morphological or pathological changes in the main organs (heart, liver, spleen, lung, and kidney) (Figure S16, Supporting Information), revealing low side effects of these therapeutic formulations. As a consequence, MCGDH can serves as a nanoplatform with friendly biosafety and biocompatibility, providing possibility for subsequent in vivo anti-tumor treatment.

Then, to explore the accumulation effect of MCGDH in tumor sites, the fluorescence intensity was tracked after Cy5.5-labeled M_{4T1}CGD, Cy5.5-labeled M_{CT26}CGD and Cy5.5-labeled CGDMSN (abbreviated as M_{4T1}CGD, M_{CT26}CGD, CGD, respectively) being intravenously injected into 4T1 tumor-bearing mice. Small-animal living imaging and the corresponding quantitative analysis revealed that the fluorescence intensity in the tumor sites of the M_{4T1}CGD group was higher than that of the M_{CT26}CGD group and the CGD group at each time point (**Figure 5a,c**), demonstrating the stronger accumulation effect of M_{4T1}CGD in 4T1 tumor-bearing mice. The ex vivo fluorescence biodistribution of isolated tumors and the main organs further demonstrated that M_{4T1}CGD had more dramatical accumulation in tumor tissues than CGD or M_{CT26}CGD (Figure 5b; Figure S17, Supporting Information). These results confirmed that the homologous targeting ability of MCGDH provided a driving force for achieving accurate anti-tumor effects of the dual-responsive nanoreactor.

Encouraged by the above research, the anti-tumor effect evoked by MCGDH was assessed according to the timeline in Figure 5d. Following the intravenous administration of these therapeutic formulations, the mice were monitored for tumor volume and body weight every other day. Compared with the control group, the tumor growth of the MDH + Cu^{2+} group was

suppressed barely, as the free copper ion failed to effectively target the tumor site. Whereas CGDH exhibited certain tumor suppression, confirming in situ formation of Cu(8-HQ)$_2$ triggered the tumor cell death. Furthermore, MCGDH showed superior anti-tumor efficacy compared to CGDH, attributed to the excellent homologous targeting of the CMs on the surface of CGDH, enabling a more efficient delivery of therapeutic agents to the tumor tissue. (Figure 5e,f). Consistently, MCGDH substantially extended the lifespan of tumor-bearing mice compared to the other groups (Figure 5h). Moreover, H&E staining revealed notable nucleus condensation and necrotic damage in the MCGDH group (Figure 5g). Besides, there was no significant change in body weight observed in mice across all treatment groups (Figure S18, Supporting Information), indicating that MCGDH did not induce systemic toxicity during anti-tumor therapy.

Next, a series of experiments were implemented to revealed the in vivo anti-tumor immune mechanism of the dual-responsive nanoreactor. As depict in Figure 5i,j, the release of HMGB1 and the surface exposure of CRT in tumor tissues of the MCGDH group were more pronounced than the other groups, suggesting that MCGDH-triggered paraptosis effectively induced the release of relevant DAMPs from 4T1 tumor cells in vivo. Additionally, the level of mDCs clipped from tumor-draining lymph nodes (TDLNs) in the MCGDH-treated group was ≈2.18-fold, 1.46-fold, 1.64-fold, and 1.27-fold of control, MGDH, MDH + Cu^{2+} and CGDH groups, respectively, since DAMPs stimulated DCs to uptake more antigen for the effective maturation (Figure 5k,m). Subsequently, we verified the activation of tumor-infiltrating cytotoxic T lymphocytes (CTLs) (CD3$^+$CD8$^+$ T cells) and helper T cells (CD3$^+$CD4$^+$ T cells) in the tumor tissues to evaluate the T cells immune responses. FCM analysis revealed that the level of CD3$^+$CD8$^+$ T cells of the MCGDH group was 3.16-fold, 1.49-fold, 1.81-fold, 1.26-fold of control, MGDH, MDH + Cu^{2+} and CGDH groups, respectively. While the level of CD3$^+$CD4$^+$ T cells of MCGDH group was also apparently enhanced compared to the other groups (Figure 5l,n,p). To further evaluate the immune activation effect, cytokines like IL-6, TNF-α and interferon-γ (INF-γ) in the serum of tumor-bearing mice following various treatments were detected by the corresponding ELISA. Notably, the secretion levels of IL-6 (Figure 5o), TNF-α (Figure 5q) and INF-γ (Figure 5r) in the MCGDH group were the highest among all groups. These encouraging results illustrated that MCGDH could evoke ICD to promote the maturation of DCs and then stimulate T cell-related immune responses for anti-tumor therapy.

2.5. Evaluation of MCGDH-Mediated Systemic Anti-Tumor Responses and Anti-Tumor Metastasis Effect

Given the the decent immune responses and therapeutic effect provoked by the enhanced immunogenicity of tumor cells mediated by MCGDH, we further determined the synergistic tumor suppression effect of MCGDH and αPD-1 in the 4T1 bilateral tumor model (**Figure 6a**). Excitingly, the combination of MCGDH and αPD-1 exhibited a more distinguished inhibition effect on primary and distant tumor growth to compared to MCGDH or αPD-1alone (Figure 6b–e). Consistently, MCGDH + αPD-1 further prolonged the surival time of mice (Figure S19, Supporting Information). H&E staining analysis of primary and distant

**ADVANCED
SCIENCE NEWS**

www.advancedsciencenews.com

**ADVANCED
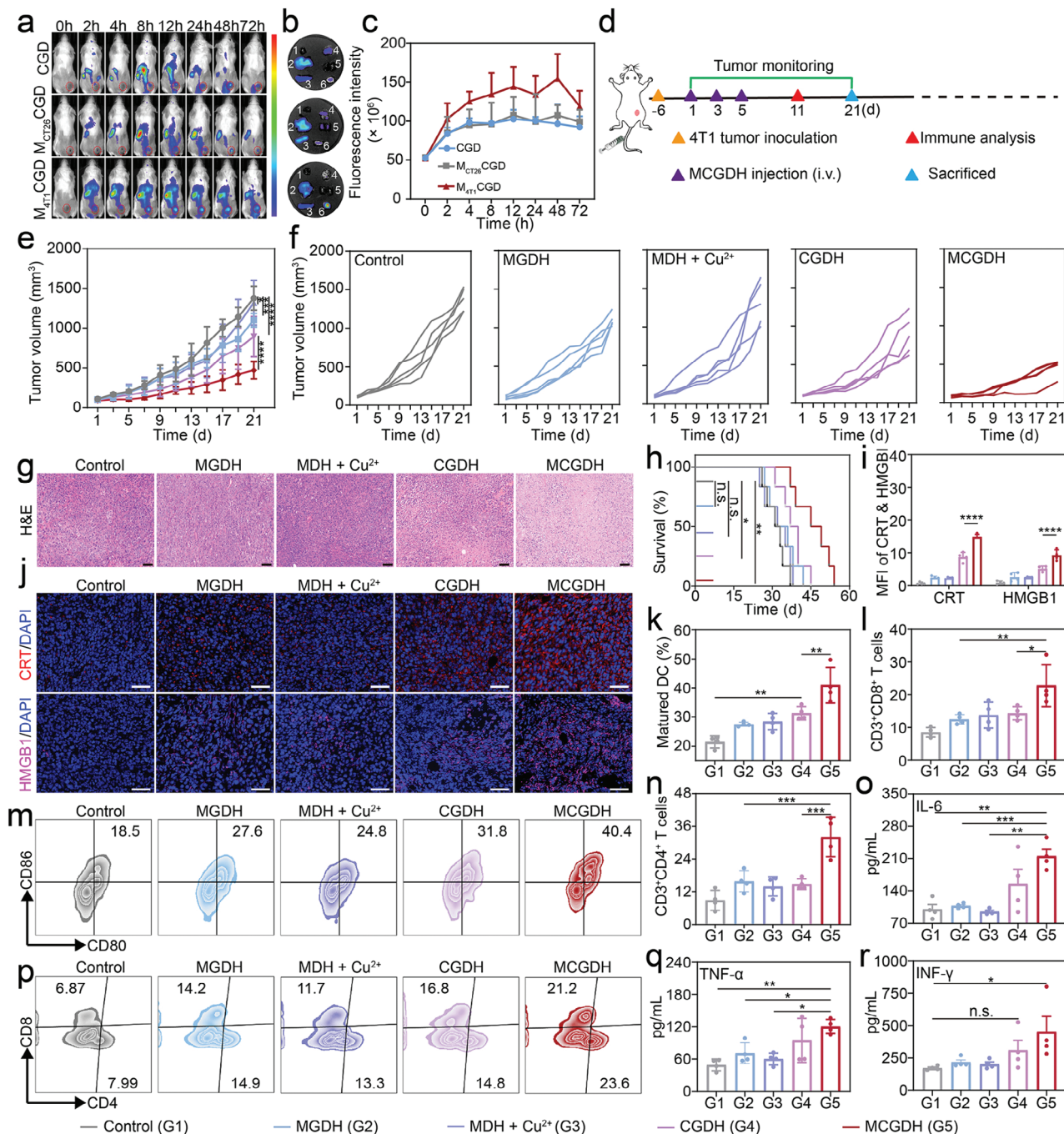FUNCTIONAL
MATERIALS**

www.afm-journal.de

Figure 5. Evaluation MCGDH-mediated anti-tumor chemo-immunotherapy effects in 4T1-tumor bearing mice. a) In vivo fluorescence imaging of 4T1 tumor-bearing mice after intravenous injection of the nanoparticles labeled by Cy5.5. b) Ex vivo fluorescence biodistribution in main organs and tumors after intravenous injection of various nanoparticles labeled by Cy5.5 for 72 h. 1: heart, 2: liver, 3: spleen, 4: lung, 5: kidney, 6: tumor. c) Quantitative fluorescence intensity analysis of tumor sites at different time points after intravenous injection of various nanoparticles labeled by Cy5.5 (n = 3). d) Schematic timeline of the therapeutic schedule of 4T1-tumor bearing mice. e) Tumor growth curves and corresponding f) tumor growth curves of each mouse after intravenous injection of various therapeutic formulations (n = 5). g) H&E staining images of tumor tissues after different treatments. Scale bar:50 μm. h) Survival rates of 4T1-tumor bearing mice after different treatments (n = 6). i) Quantitative analysis of HMGB1 and CRT in tumor tissues following various treatments (n = 4) and corresponding j) immunofluorescence staining images. Scale bar: 50 μm. Quantitative analysis of k) mature DCs in tumor-draining lymph nodes and l) CD3$^+$CD8$^+$ T cells in tumor tissues of mice after different treatments by FCM analysis (n = 4). m) Representative flow cytometry plots of mature DCs in tumor draining lymph nodes of mice after different treatments. n) Quantitative analysis of CD3$^+$CD4$^+$ T cells in tumor tissues of mice after different treatments (n = 4). o) The secretion levels of IL-6 in the serum of tumor-bearing mice after different treatments (n = 4). p) Representative flow cytometry plots of CD3$^+$CD8$^+$CD4$^+$ T cells in tumor tissues of mice after different treatments. The secretion levels of q) TNF-α and r) INF-γ in the serum of tumor-bearing mice after different treatments (n = 4). Data are represented as mean values ± SD. Significant difference was assessed by one-way ANOVA. $^*p < 0.05$, $^{**}p < 0.01$, $^{***}p < 0.001$, $^{****}p < 0.0001$, n.s. no significance.
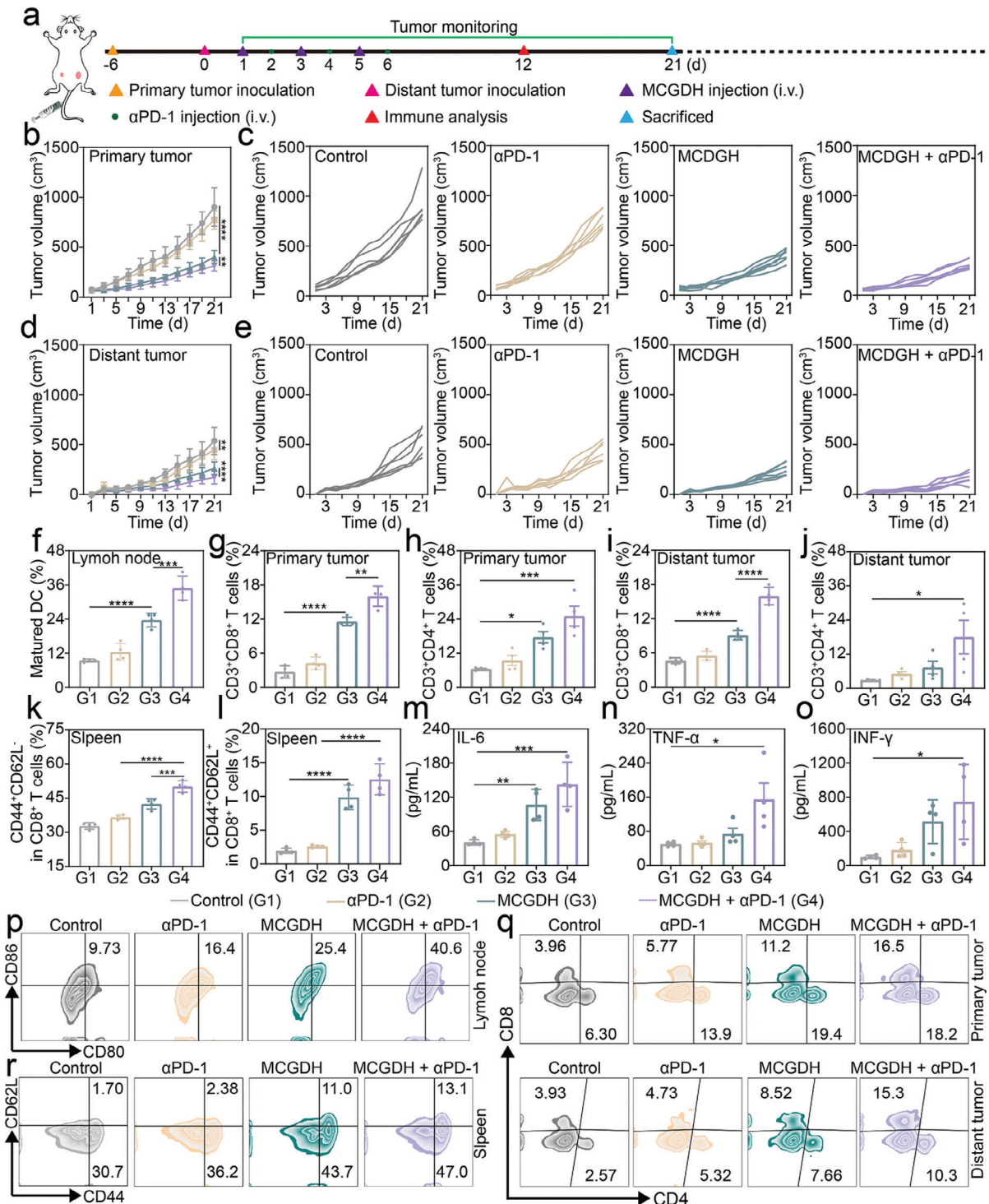
Figure 6. Evaluation of the enhanced systemic anti-tumor effect of MCGDH combined with αPD-1 in 4T1 bilateral tumor model. a) Schematic timeline of in vivo therapeutic schedule of 4T1 bilateral tumor model. b) Tumor growth curves of primary tumors and c) corresponding individual growth curves of each mouse after intravenous injection of various therapeutic formulations (n = 6). d) Tumor growth curves of distant tumors and e) corresponding individual growth curves of each mouse (n = 6). Quantitative analysis of f) mature DCs in tumor-draining lymph nodes, g) $CD3^+CD8^+$ T cells in primary tumor tissues, h) $CD3^+CD4^+$ T cells in primary tumor tissues, i) $CD3^+CD8^+$ T cells in distant tumor tissues, j) $CD3^+CD4^+$ T cells in distant tumor, k) T_{EM} ($CD8^+CD44^+CD62L^-$) cells and l) T_{CM} ($CD8^+CD44^+CD62L^+$) cells in spleens after different treatments by FCM analysis (n = 4). The secretion levels of m) IL-6, n) TNF-α and o) INF-γ in the serum of 4T1 bilateral tumor-bearing mice after different treatments (n = 4). Representative flow cytometry plots of p) mature DCs in tumor draining lymph nodes, q) $CD3^+CD8^+$ T cells and $CD3^+CD4^+$ T cells in primary and distant tumor tissues, r) T_{CM} and T_{EM} cells in spleens after different treatments. Data are represented as mean values ± SD. Significant difference was assessed by one-way ANOVA. $^*p < 0.05$, $^{**}p < 0.01$, $^{***}p < 0.001$, $^{****}p < 0.0001$, n.s. no significance.

**ADVANCED
SCIENCE NEWS**

www.advancedsciencenews.com

**ADVANCED
FUNCTIONAL
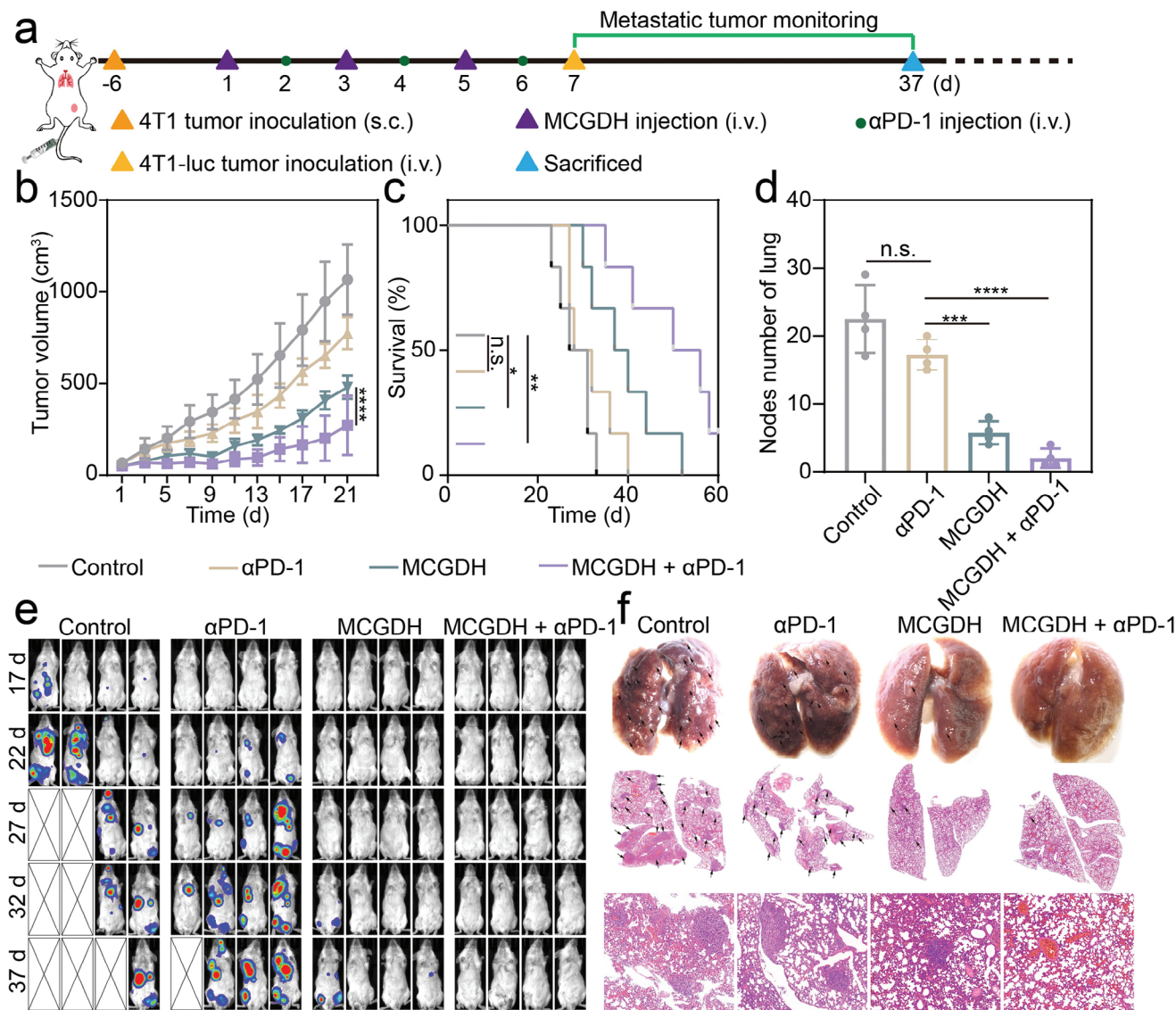MATERIALS**

www.afm-journal.de

Figure 7. Evaluation of the anti-metastasis effect of MCGDH combined with αPD-1. a) Schematic timeline of the therapeutic profile for the metastatic 4T1 tumor model. b) Tumor growth curves of subcutaneous tumors and c) survival rates of mice after different treatments (n = 6). d) Quantitative counting of metastatic lung nodes. e) Bioluminescence images of mice after the injection of 4T1-luc tumor cells at different periods. f) Photographs and H&E staining of lung tissues after various treatments. Down: scale bar: 200 μm. Data are represented as mean values ± SD. Significant difference was assessed by one-way ANOVA. $^*p < 0.05$, $^{**}p < 0.01$, $^{***}p < 0.001$, $^{****}p < 0.0001$, n.s. no significance.

tumor tissues revealed the most substantially damaged and dead tumor cells of MCGDH + αPD-1-treated mice (Figure S20, Supporting Information). Meanwhile, negligible body weight change of these four groups was detected during the treatment period (Figure S21, Supporting Information), suggesting negligible systemic toxicity of the synergistic treatment. All these results confirmed the synergistic action of MCGDH + αPD-1 for tumor suppression.

To evaluate the immune activation effect of MCGDH + αPD-1, the immune-related indicators, including mDCs in TDLNs, tumor-infiltraing $CD3^+CD8^+$ T cells, $CD3^+CD4^+$ T cells and effector memory T cells (T_{EM}) ($CD8^+CD44^+CD62L^-$) as well as central memory T cells (T_{CM}) ($CD8^+CD44^+CD62L^+$) were demonstrated via FCM analysis. Specifically, the percentage of mDCs in

TDLNs was 40.6% in the MCGDH + αPD-1-treated group, which was 1.60-fold, 2.48-fold, 4.17-fold of MCGDH (25.4%), αPD-1 (16.4%) and control (9.73%) groups, respectively (Figure 6f,p), indicating that MCGDH + αPD-1 promoted the effective DC maturation. Furthermore, the percentages of $CD3^+CD8^+$ T cells and $CD3^+CD4^+$ T cells were 16.5% and 18.2% in the primary tumor, 15.3% and 10.3% in the distant tumor, which were higher than those of the other groups (Figure 6g–j,q). Consistent results from the immuno-histochemical images showed that MCGDH + αPD-1 effectively increased the activation of CTLs to secrete granzyme B in distant tumors (Figure S22, Supporting Information), since the robust systemic immune responses of the combination therapy excited the infiltration of CTLs. In addition, the percentages of T_{EM} cells and T_{CM} cells in the spleens

of the MCGDH + αPD-1 group were 47.0% and 13.1%, respectively, which was significantly higher than that of the MCGDH group (43.7% and 11.0%), αPD-1 group (36.2% and 2.38%) and control groups (30.7% and 1.70%) (Figure 6k,l,r), indicating that MCGDH + αPD-1 effectively activated long-term immunological effects to inhibit the progression of distant tumors. Notably, the levels of cytokines including IL-6, TNF-α and INF-γ in the serum of the MCGDH + αPD-1-treated group were also remarkably elevated than the other three groups (Figure 6m–o), which further verified the synergistic treatment with MCGDH and αPD-1 could induce vigorous systemic immune responses to efficiently eliminate bilateral tumor cells.

The systemic immune responses induced by the combination of MCGDH and αPD-1 encouraged us to further evaluate its effects on inhibiting tumor metastasis. The tumor metastasis model was established as depicted in **Figure** 7a. Consistent with the aforementioned results, MCGDH + αPD-1 amplified the the therapeutic effect against subcutaneous tumors (Figure 7b; Figure S23, Supporting Information). The metastatic dissemination of luciferase-4T1 (4T1-luc) tumor cells was monitored by a bioluminescence imaging system. As illustrated in Figure 7e, the luminous sites in the lung tissues of the control group mice appeared the earliest, with these mice experiencing the fastest mortality, indicating severe metastases. In comparison, the metastasis of αPD-1-treated mice was slightly delayed, while MCGDH-treated mice exhibited significant inhibition of metastasis. Encouragingly, the anti-metastasis effect of MCGDH + αPD-1 was superior to that of MCGDH alone. The representative photos and H&E straning revealed that the absence of metastatic tumor nodules in the lung tissues of the MCGDH + αPD-1 group, while sporadic metastatic lesions were observed in the lung tissues of MCGDH-treated mice. In contrast, the lung tissues of the control group and αPD-1 group showed plenteous metastatic lesions (Figure 7d,f). Comfortingly, the survival rate of mice of the MCGDH + αPD-1 group was signally prolonged, with a median surival time of 53 d, which was 1.38-fold, 1.77-fold, 1.83-fold longer than that of the MCGDH (38.5 d), αPD-1 (30 d) and contorl groups (29 d), respectively (Figure 7c). These consistent results confirmed that ICB therapy effectively enhanced the efficacy of MCGDH-mediated anti-tumor metastasis.

3. Conclusion

In summary, a GSH/pH dual-responsive nanoreactor (MCGDH) was constructed for in situ synthesis of anti-tumor activity Cu(8-HQ)$_2$. The homologous targeting ability of CMs promoted more efficient endocytosis of MCGDH by 4T1 cells. Subsequently, the acidic condition and high concentration of GSH in the tumor microenvironment triggered the release of Cu^{2+} and 8-HQ from MCGDH, leading to in situ formation of Cu(8-HQ)$_2$ and initiating tumor cell paraptosis. The paraptosis process amplified the immunogenicity of tumor cells by inducing ER stress and ROS production, which resulted in potent anti-tumor immune responses. Furthermore, in vivo studies validated that the combination of MCGDH and αPD-1 could synergistically enhance the systemic anti-tumor immune responses and provide long-term immunological effects, inhibiting the growth of distant tumors and preventing tumor metastasis. With the flexibility to substitute doped metal ions and loaded drugs in MCGDH, this dual-responsive nanoreactor serves as a versatile platform for chemo-immunotherapy, promising to enhance the therapeutic efficacy of ICB therapy.

4. Experimental Section

Methods and any associated references are available in the Supporting Information.

Supporting Information

Supporting Information is available from the Wiley Online Library or from the author.

Conflict of Interest

The authors declare no conflict of interest.

Data Availability Statement

The data that support the findings of this study are available from the corresponding author upon reasonable request.

[1] a) N. M. Kuderer, A. Desai, M. B. Lustberg, G. H. Lyman, *Nat. Rev. Clin. Oncol.* **2022**, *19*, 681; b) M. Tian, D. Y. Fan, Z. Liu, X. Mu, Q. Q. Tao, C. Y. Yu, S. Y. Zhang, *Adv. Mater.* **2022**, *34*, 2205299.

[2] a) Y. Tang, H. K. Bisoyi, X.-M. Chen, Z. Liu, X. Chen, S. Zhang, Q. Li, *Adv. Mater.* **2023**, *35*, 2300232; b) D. R. Green, T. Ferguson, L. Zitvogel, G. Kroemer, *Nat. Rev. Immunol.* **2009**, *9*, 353; c) W. Xu, J. Qian, G. Hou, T. Wang, J. Wang, Y. Wang, L. Yang, X. Cui, A. Suo, *Adv. Funct. Mater.* **2022**, *32*, 2205013.

[3] a) W. Gao, X. Wang, Y. Zhou, X. Wang, Y. Yu, *Signal Transduct. Targeted Ther.* **2022**, *7*, 196; b) A. Linkermann, B. R. Stockwell, S. Krautwald, H.-J. Anders, *Nat. Rev. Immunol.* **2014**, *14*, 759.

[4] a) G.-N. Li, X.-J. Zhao, Z. Wang, M.-S. Luo, S.-N. Shi, D.-M. Yan, H.-Y. Li, J.-H. Liu, Y. Yang, J.-H. Tan, Z.-Y. Zhang, R.-Q. Chen, H.-L. Lai, X.-Y. Huang, J.-F. Zhou, D. Ma, Y. Fang, Q.-L. Gao, *Signal Transduct. Targeted Ther.* **2022**, *7*, 317; b) X. Liu, Y. Gu, Y. Bian, D. Cai, Y. Li, Y. Zhao, Z. Zhang, M. Xue, L. Zhang, *Apoptosis* **2021**, *26*, 195.

[5] a) J. K. Mandula, S. Chang, E. Mohamed, R. Jimenez, R. A. Sierra-Mondragon, D. C. Chang, A. N. Obermayer, C. M. Moran-Segura, S. Das, J. A. Vazquez-Martinez, K. Prieto, A. Chen, K. S. M. Smalley, B. Czerniecki, P. Forsyth, R. C. Koya, B. Ruffell, J. R. Cubillos-Ruiz, D. H. Munn, T. I. Shaw, J. R. Conejo-Garcia, P. C. Rodriguez, *Cancer Cell* **2022**, *40*, 1145; b) F. Fontana, M. Raimondi, M. Marzagalli, A. Di Domizio, P. Limonta, *Biochim. Biophys. Acta - Rev. Cancer.* **2020**, *1873*, 188338.

[6] a) H. Ma, Y. Lu, Z. Huang, S. Long, J. Cao, Z. Zhang, X. Zhou, C. Shi, W. Sun, J. Du, J. Fan, X. Peng, *J. Am. Chem. Soc.* **2022**, *144*, 3477; b) L. Zhang, N. Montesdeoca, J. Karges, H. Xiao, *Angew. Chem., Int. Ed.* **2023**, *62*, e202300662; c) D. Li, S. Liu, Y. Ma, S. Liu, Y. Liu, J. Ding, *Small Methods* **2023**, *7*, 2300204.

[7] R.-R. Zheng, L.-P. Zhao, C.-Y. Huang, H. Cheng, N. Yang, Z.-X. Chen, H. Cai, W. Zhang, R.-J. Kong, S.-Y. Li, *ACS Nano* **2023**, *17*, 9972.

[8] a) L. Galluzzi, J. Humeau, A. Buqué, L. Zitvogel, G. Kroemer, *Nat. Rev. Clin. Oncol.* **2020**, *17*, 725; b) R. Kuai, W. Yuan, S. Son, J. Nam, Y. Xu, Y. Fan, A. Schwendeman, J. J. Moon, *Sci. Adv.* **2018**, *4*, eaao1736; c) S. Jia, Z. Gao, Z. Wu, H. Gao, H. Wang, H. Ou, D. Ding, *CCS Chem.* **2021**, *4*, 501.

[9] a) L. He, K. N. Wang, Y. Zheng, J. J. Cao, M. F. Zhang, C. P. Tan, L. N. Ji, Z. W. Mao, *Dalton. Trans.* **2018**, *47*, 6942; b) F. Wei, J. Karges, S. Gao, L. Wang, X. Zhang, X.-C. Shen, L. Ji, H. Chao, *Nano Today* **2024**, *54*, 102066; c) Z. Guo, X. Gao, J. Lu, Y. Li, Z. Jin, A. Fahad, N. U. Pambe, H. Ejima, X. Sun, X. Wang, W. Xie, G. Zhang, L. Zhao, *ACS Nano* **2024**, *18*, 6975.

[10] a) P. Tsvetkov, S. Coy, B. Petrova, M. Dreishpoon, A. Verma, M. Abdusamad, J. Rossen, M. Joesch-Cohen, R. Humeidi, R. D. Spangler, J. K. Eaton, E. Frenkel, M. Kocak, S. M. Corsello, S. Lutsenko, N. Kanarek, S. Santagata, T. R. Golub, *Science* **2022**, *375*, 1254; b) Y. Jiang, Z. Huo, X. Qi, T. Zuo, Z. Wu, *Nanomedicine-UK* **2022**, *17*, 303.

[11] a) T. Li, Y. Zhang, J. Zhu, F. Zhang, A. a. Xu, T. Zhou, Y. Li, M. Liu, H. Ke, T. Yang, Y. a. Tang, J. Tao, L. Miao, Y. Deng, H. Chen, *Adv. Mater.* **2023**, *35*, 2210201; b) W. Wu, L. Yu, Y. Pu, H. Yao, Y. Chen, J. Shi, *Adv. Mater.* **2020**, *32*, 2000542; c) Q. X. Huang, J. L. Liang, Q. W. Chen, X. K. Jin, M. T. Niu, C. Y. Dong, X. Z. Zhang, *Nano Today* **2023**, *51*, 101911; d) X. K. Jin, J. L. Liang, S. M. Zhang, Q. X. Huang, S. K. Zhang, C. J. Liu, X. Z. Zhang, *Mater. Today* **2023**, *68*, 108.

[12] Q. Peña, A. Wang, O. Zaremba, Y. Shi, H. W. Scheeren, J. M. Metselaar, F. Kiessling, R. M. Pallares, S. Wuttke, T. Lammers, *Chem. Soc. Rev.* **2022**, *51*, 2544.

[13] a) A. Barilli, C. Atzeri, I. Bassanetti, F. Ingoglia, V. Dall'Asta, O. Bussolati, M. Maffini, C. Mucchino, L. Marchiò, *Mol. Pharmaceut.* **2014**, *11*, 1151; b) Y. Zhou, F. Huang, Y. Yang, P. Wang, Z. Zhang, Y. Tang, Y. Shen, K. Wang, *Small* **2018**, *14*, 1702446.

[14] a) Y. Yang, M. Zhang, Y. Yang, D. Cheng, C. Yu, *Angew. Chem., Int. Ed.* **2021**, *60*, 11504; b) G. F. Luo, W. H. Chen, X. Z. Zhang, *Chin. J. Chem.* **2023**, *42*, 1175; c) J. L. Liang, X. K. Jin, S. M. Zhang, Q. X. Huang, P. Ji, X. C. Deng, S. X. Cheng, W. H. Chen, X. Z. Zhang, *Sci. Bull.* **2023**, *68*, 622; d) X. K. Jin, S. M. Zhang, J. L. Liang, S. K. Zhang, Y. T. Qin, Q. X. Huang, C. J. Liu, X. Z. Zhang, *Adv. Mater.* **2024**, *36*, 2309094; e) F. Gao, Q. Cheng, M. D. Liu, L. Rong, C. J. Liu, X. Z. Zhang, *Sci. China Chem.* **2019**, *62*, 1230.

[15] a) L. Yu, Y. Chen, M. Wu, X. Cai, H. Yao, L. Zhang, H. Chen, J. Shi, *J. Am. Chem. Soc.* **2016**, *138*, 9881; b) M. Vallet-Regí, F. Schüth, D. Lozano, M. Colilla, M. Manzano, *Chem. Soc. Rev.* **2022**, *51*, 5365; c) W. Wu, L. Yu, Q. Jiang, M. Huo, H. Lin, L. Wang, Y. Chen, J. Shi, *J. Am. Chem. Soc.* **2019**, *141*, 11531; d) J. G. Croissant, Y. Fatieiev, N. M. Khashab, *Adv. Mater.* **2017**, *29*, 1604634.

[16] a) S. Y. Peng, X. H. Liu, Q. W. Chen, Y. J. Yu, M. D. Liu, X. Z. Zhang, *Biomaterials* **2022**, *281*, 121358; b) Y. Huang, S. Wu, L. Zhang, Q. Deng, J. Ren, X. Qu, *ACS Nano* **2022**, *16*, 4228; c) C. Wang, F. Cao, Y. Ruan, X. Jia, W. Zhen, X. Jiang, *Angew. Chem., Int. Ed.* **2019**, *58*, 9846; d) B. Niu, K. Liao, Y. Zhou, T. Wen, G. Quan, X. Pan, C. Wu, *Biomaterials* **2021**, *277*, 121110.

[17] a) T. Li, G. Chen, Z. Xiao, B. Li, H. Zhong, M. Lin, Y. Cai, J. Huang, X. Xie, X. Shuai, *Nano Lett.* **2022**, *22*, 3095; b) X. F. Bai, Y. Chen, M. Z. Zou, C.-X. Li, Y. Zhang, M. J. Li, S. X. Cheng, X. Z. Zhang, *ACS Nano* **2022**, *16*, 18555; c) R. H. Fang, W. Gao, L. Zhang, *Nat. Rev. Clin. Oncol.* **2023**, *20*, 33.

[18] a) V. F. S. Pape, A. Gaál, I. Szatmári, N. Kucsma, N. Szoboszlai, C. Streli, F. Fülöp, É. A. Enyedy, G. Szakács, *Cancers* **2021**, *13*, 154; b) S. Tardito, A. Barilli, I. Bassanetti, M. Tegoni, O. Bussolati, R. Franchi-Gazzola, C. Mucchino, L. Marchiò, *J. Med. Chem.* **2012**, *55*, 10448.

[19] a) G. Kroemer, C. Galassi, L. Zitvogel, L. Galluzzi, *Nat. Immunol.* **2022**, *23*, 487; b) Y. Zhang, X. Hou, S. Du, Y. Xue, J. Yan, D. D. Kang, Y. Zhong, C. Wang, B. Deng, D. W. McComb, Y. Dong, *Nat. Nanotechnol.* **2023**, *18*, 1364; c) Y. T. Qin, X. H. Liu, J. X. An, J. L. Liang, C. X. Li, X. K. Jin, P. Ji, X. Z. Zhang, *ACS Nano* **2023**, *17*, 24947.

[20] Z. H. Li, Y. Chen, X. Zeng, X. Z. Zhang, *Nano Today* **2021**, *38*, 101150.

[21] K. Wang, Y. Li, X. Wang, Z. Zhang, L. Cao, X. Fan, B. Wan, F. Liu, X. Zhang, Z. He, Y. Zhou, D. Wang, J. Sun, X. Chen, *Nat. Commun.* **2023**, *14*, 2950.

[22] L. Ma, X. Xuan, M. Fan, Y. Zhang, G. Yuan, G. Huang, Z. Liu, *Apoptosis* **2022**, *27*, 577.